

# Probing anyonic statistics via Mach-Zehnder interferometry in quantum computers

Shiyu Zhou,<sup>1,2</sup> Yi Teng,<sup>3</sup> Claudio Chamon,<sup>1</sup> Claudio Castelnovo,<sup>3</sup> and Armin Rahmani<sup>4</sup>

<sup>1</sup>*Department of Physics, Boston University, Boston, MA, 02215, USA*

<sup>2</sup>*Perimeter Institute for Theoretical Physics, Waterloo, Ontario, Canada N2L 2Y5*

<sup>3</sup>*TCM Group, Cavendish Laboratory, University of Cambridge, Cambridge CB3 0HE, UK*

<sup>4</sup>*Department of Physics and Astronomy and Advanced Materials Science and Engineering Center, Western Washington University, Bellingham, Washington 98225, USA*

We introduce a synthetic Mach-Zehnder interferometer for digitized quantum computing devices to probe fractional exchange statistics of anyonic excitations that appear in quantum spin liquids. Employing an IonQ quantum computer, we apply this scheme to the toric ladder, a quasi-one-dimensional reduction of the toric code. We observe interference patterns resulting from the movement of ‘electric’ excitations in the presence and absence of ‘magnetic’ ones. We model the noise in IonQ via depolarizing Lindbladian dynamics, and find quantitative agreement with the measurements obtained from the quantum device. The synthetic Mach-Zehnder interferometer can thus also serve as an effective means to probe the coherence length and time scales of multi-qubit noisy quantum devices.

*Introduction* - The use of interferometry as an experimental tool has led to multiple important discoveries in physics. For example, the Michelson interferometer was the basis for the Michelson and Morley experiment [1] that demonstrated that light travels at the same speed along perpendicular directions, contradicting the existence of a medium – the ether – through which light was thought to propagate. Combinations of Michelson and Fabry-Pérot [2, 3] interferometers were essential for the detection of gravitational waves [4]. Interferometry has also been applied to particle systems, notably on recent experiments using Fabry-Pérot interferometers that demonstrated fractional exchange statistics of quasiparticles of certain quantum Hall states [5–7]. Other interferometric geometries that aim at detecting fractional exchange statistics in quantum Hall states, such as Mach-Zehnder interferometers, have also been theoretically studied [8, 9] and experimentally realized [10].

In this paper we develop a synthetic Mach-Zehnder interferometer to demonstrate fractional exchange statistics of excitations in topological states of matter [11] realizable in quantum simulators and quantum computers [12–14]. Examples of such topological systems are quantum spin liquids<sup>1</sup>, which are a central topic in quantum many-body physics, but are hard to realize in materials-based systems [17, 18]. There has been much effort and success in implementing such states in existing quantum devices [19, 20]. Here we focus on simulating the nonequilibrium dynamics of the fractionalized excitations of quantum spin liquids generated by a time-independent Hamiltonian, as opposed to the more conventional route of generating the quantum states that mimic the ground states of quantum spin liquids and adi-

abatically manipulating its excitations.

Our setup is characterized by the following features: (1) the qubits in the quantum device are in one-to-one correspondence with the physical degrees of freedom of the model that hosts the anyonic excitations; and (2) the quantum circuit directly executes a Trotterized representation of unitary evolution based on the time-independent Hamiltonian of the model. The significance of our method rests in its ability to leverage synthetic quantum platforms for a faithful emulation and identification of the distinctive signatures of anyonic statistics during nonequilibrium quantum evolution. An interesting dual aspect of our work, as we illustrate and discuss below, is that one can use artificial quasiparticle Mach-Zehnder interferometry as a means to assess the coherence length and time scales of quantum computing and quantum simulation platforms, and gain insight into the nature and strength of their intrinsic noise.

As a concrete demonstration of the approach, we study a quasi-1D ladder variant of the toric code [21], which hosts two types of excitations, spinons and visons, or ‘electric’ and ‘magnetic’ charges. The two types of excitations behave as mutual semions, picking up a phase  $\pi$  as one is moved around the other. We implement this construction on the IonQ quantum device, and successfully observe signatures of the mutual semionic statistics in the propagation of spinons in the presence or absence of a background of visons.

*Toric ladder* - The two-dimensional Kitaev’s toric code [21] is a canonical example of a topologically ordered state supporting two types of anyonic excitations. The toric-code ground state is the simultaneous eigenstate of star and plaquette operators with eigenvalue 1. Stars and plaquettes with eigenvalue  $-1$ , respectively, correspond to ‘electric’ and ‘magnetic’ excitations, also known as spinons and visons. While these two species are bosonic with respect to themselves, they have mutual semionic statistics, whereby braiding one around the

<sup>1</sup> For an alternative recent proposal to use interferometry of thermal currents of anyonic excitations to probe fractional statistics in quantum spin liquids see Refs. 15 and 16.

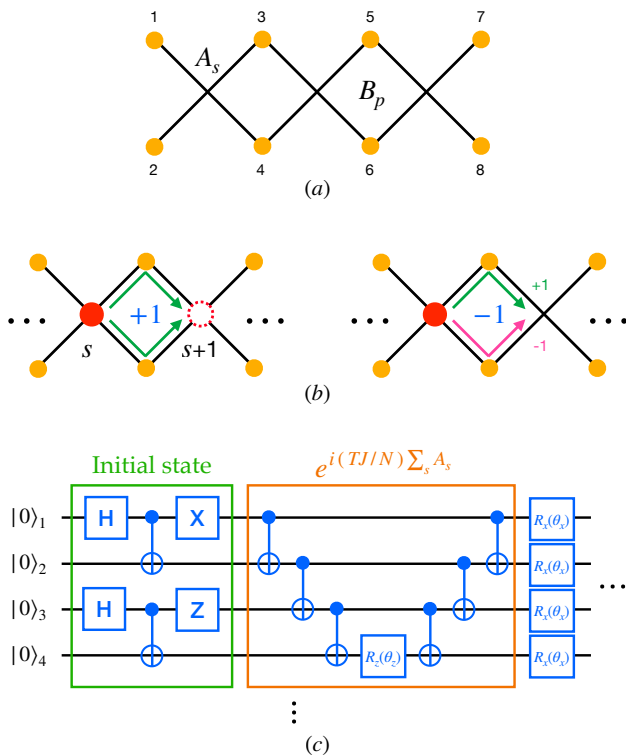


FIG. 1. (a) The geometry of a toric ladder of 3 stars  $A_s$ , which can be easily extended to a ladder of arbitrary length. Two plaquettes  $B_p$  are sandwiched between adjacent stars, and two lie at the edges of the ladder. (b) A spinon initialized at star  $s$  ( $A_s = -1$ ), upon the action of a transverse field, is able to hop say to the star at  $s + 1$  based on whether a vison is present in the plaquette in between ( $B_p = +1$  or  $B_p = -1$ ). (c) The circuit layout for emulating a Mach-Zehnder interferometer using a toric ladder Eq. (1) of 3 stars. The circuit consists of two stages: (1) preparation of an initial state with a spinon and with/without a vison, shown in the green box; (2) implementation of the Trotterized Hamiltonian evolution of Eq. (1). Specifically, the execution of one time evolution step of the star operator is shown in the orange box.

other imparts a phase  $\pi$  to the wave function.

In the toric code, these excitations are static and their nontrivial mutual statistics only plays a role when they are externally manipulated and braided. However, applying small (compared with the gap so as not to drive the system into a conventionally ordered phase) external fields leads to the hopping of these excitations on the lattice. The semionic statistics then manifests in a prominent way [22–24], underpinned by a mechanism that can be most easily understood at the single plaquette level. When a vison occupies a plaquette of the square lattice, the coherent motion of a spinon from one corner of the plaquette to the diagonally opposite one is governed by the interference of the two trajectories going around to the left and to the right of the plaquette. Mutual semionic statistics causes perfect destructive interference, leading to a vanishing spinon wave function at

the opposite corner. Therefore, spinon motion is entirely obstructed by the presence of the vison.

Here we want to construct a minimal model where the effects of mutual statistics on quasiparticle motion are most dramatic, and thence most easily detected. Consider the  $i = 1, \dots, 8$  spin-1/2 ‘toric ladder’ illustrated in Fig. 1(a) (which can be trivially extended to a ladder of arbitrary length). It encompasses three crosses, or stars  $s = 1, 2, 3$ , where we define star operators  $A_s = \prod_{i \in s} \sigma_i^z$  (i.e., the product of the  $z$  Pauli matrices of the 4 adjacent spins,  $i \in s$ ), and four plaquettes (formed of 2 spins each), two sandwiched between adjacent stars and two at the edges of the ladder. Let us define the Hamiltonian

$$H = -\lambda \sum_s A_s - \Gamma \sum_j \sigma_j^x, \quad (1)$$

where in the following  $\lambda = 1$  will be our reference dominant energy scale, and  $\Gamma \ll 1$  can be assumed positive without loss of generality. The Hamiltonian commutes with 4 plaquette operators,  $B_p = \sigma_{2p-1}^x \sigma_{2p}^x$  for  $p = 1, 2, 3, 4$ , and with one string operator,  $\prod_i \sigma_{2i-1}^x$ . One can verify that these are all independent and that there are no further commuting independent operators built purely of  $x$  Pauli matrices in the system. The string operator labels different topological sectors, which exhibit identical interferometric behavior. We thus focus on one topological sector. The same is true about  $B_1 = \sigma_1^x \sigma_2^x$  and  $B_4 = \sigma_7^x \sigma_8^x$ . On the contrary,  $B_{2,3} = \pm 1$  crucially identify the presence/absence of visons in the two central (complete) plaquettes in Fig. 1(a). We will focus in particular on the cases of no visons ( $B_{2,3} = +1$ ), and of a single vison on the left or right central plaquette ( $B_2 = -1, B_3 = +1$  or  $B_2 = +1, B_3 = -1$ ).

Overall, the  $2^8$  dimensional Hilbert space is broken down into  $2^3$  dimensional block-diagonal sectors, which are spanned by the spinon number eigenstates, labelled by  $A_{1,2,3} = \pm 1$ . Note that the star operators  $A_s$  do not commute with the Hamiltonian due to the presence of a transverse field  $\Gamma$ . However, given that their coupling constant (namely, the spinon energy cost) is dominant in our system<sup>2</sup>, different spinon number sectors are well separated in energy and one can gain useful insight into the behaviour of the system by working at fixed spinon number. The sector of primary interest in our work will be the single spinon sector, where the transverse field  $\Gamma$  can be seen as a hopping term for the spinon along the toric ladder. Notably, a spinon prepared at a given star  $s$  can hop, say, to  $s + 1$  by acting with the transverse field on the spin along the top or the bottom leg of the ladder, and the overall motion is given by the interference of the two trajectories, on either side of the intervening plaquette  $p$ . This is where  $B_p = +1$  (no vison) leads to perfect

<sup>2</sup> This statement shall remain true even when we consider coupling to a bath later on.

constructive interference, and  $B_p = -1$  (vison) leads to perfect destructive interference: the spinon is unable to move along the ladder if a vison is present in the adjacent plaquette, as shown in Fig. 1 (b).

To put all this to the test, we contrast the behaviour of quantum quenches that start from a state with a single spinon localised on the leftmost star ( $A_1 = -1$ ,  $A_{2,3} = +1$ ), and three distinct vison number eigenstates: (i) no vison ( $B_{2,3} = +1$ ); (ii) a single vison on the centre-left plaquette ( $B_2 = -1$ ,  $B_3 = +1$ ); and (iii) a single vison on the centre-right plaquette ( $B_2 = +1$ ,  $B_3 = -1$ )<sup>3</sup>. In the extreme scenario where spinon number sectors are completely separated in energy, the Hamiltonian time evolution leads to a static spinon at  $s = 1$  in case (ii), a delocalized spinon all stars in case (i), and a delocalized spinon across  $s = 1, 2$  in case (iii). We will then compare this ideal Mach-Zehnder interferometer setup to situations where energy scales are finite and noise is present in the system, as appropriate for any implementation in a noisy quantum device.

*Quantum device implementation* - We use the IonQ Aria quantum device<sup>4</sup> available in the AWS Braket to emulate the Mach-Zehner interferometer. Specifically, we first prepare an initial state with a spinon and with/without a vison, and then simulate the Trotterized time evolution according to the Hamiltonian in Eq. (1) of the quantum quench discussed in the previous section. We use the IonQ Aria quantum device<sup>5</sup> available in the AWS Braket to emulate the Mach-Zehner interferometer. Specifically, we first prepare an initial state with a spinon and with/without a vison, and then simulate the Trotterized time evolution according to the Hamiltonian in Eq. (1) of the quantum quench discussed in the previous section.

The starting state of the Aria quantum device  $|0\rangle^{\otimes 8}$  (i.e., all qubits polarised in the positive  $z$  direction) satisfies the condition of all plaquette operators  $B_p$  having eigenvalue  $+1$ . We can then set all star operators  $A_s$  to have eigenvalue  $+1$  by applying a Hadamard gate to each odd qubit, namely along the top leg of the ladder in Fig. 1(a), and following it by a sequence of CNOT gates, see Fig. 1(c). The spinon at star  $s = 1$  is then initialised by applying an  $X$  gate to one of the left boundary qubits, and the vison can be created by applying a  $Z$  gate to one of the qubits (on the top or bottom leg) at the desired plaquette. The circuit layout to implement the initial state is shown in the green box in Fig. 1(c).

In order to simulate the time evolution of a given initial state according to the Hamiltonian Eq. (1) in the digital quantum device, we use Trotterization:

$$e^{-iHt} = e^{-i(-\lambda \sum_s A_s - \Gamma \sum_j \sigma_j^x)t} \\ \simeq \left( e^{i\frac{t\lambda}{n} \sum_s A_s} e^{i\frac{t\Gamma}{n} \sum_j \sigma_j^x} \right)^n, \quad n \gg 1$$

where  $\hbar$  is set to 1. This becomes exact in the limit of number of Trotter steps  $n \rightarrow \infty$ . However, the noisy nature of quantum devices and their limited coherence time impose a strong preference for shallow circuits. For this reason, we numerically compare the exact diagonalisation time evolution with Trotterised evolution to find the smallest number of steps which gives us an approximation error less than 15% (see Supplementary Material for details). We then use this as our optimal value  $n_{\text{opt}}$  in the quantum device implementation. For the 8-spin toric ladder and total time  $T = 10$  (with  $\lambda = 1$  and  $\Gamma = 0.1$ ), we find the optimal number of Trotter steps to be  $n_{\text{opt}} = 8$ . Fig. 2 (top row) compares the time evolution simulated from both exact diagonalization and Trotterization.

In order to implement the time evolution associated with the star operators in the Hamiltonian,  $e^{i\frac{t\lambda}{n} A_s}$ , we decompose it into a series of quantum gates consisting of CNOT gates and  $\text{Rz}(\theta_z)$  gates that rotate the qubit about the  $z$ -axis by an angle  $\theta_z = \frac{-t\lambda}{n}$ , shown in the orange box in Fig. 1(b). The transverse field evolution  $e^{i\frac{t\Gamma}{n} \sigma_j^x}$  is just the  $\text{Rx}(\theta_x)$  gate that rotates the qubit about the  $x$ -axis by an angle  $\theta_x = \frac{-t\Gamma}{n}$ .

*Results* - We show in Fig. 2 the simulation results of a single spinon propagating in the background of different vison arrangements. The total time is  $T = 10$ , and at each intermediate time step, we measure the expectation value of the star operators  $\langle A_s \rangle$  at all sites  $s = 1, 2, 3$ , effectively tracking the location of the spinon as a function of time. The upper row displays the exact time evolution in comparison to the Trotterized one. We reaffirm the Mach-Zehnder interferometry-type behavior discussed earlier: the extent to which the spinon is able to propagate is determined by the interference pattern arising from the mutual semionic statistics of the spinon and the vison. The middle plot shows that the spinon propagation stops in the presence of an adjacent vison, contrasted to the left plot where no vison is present, allowing the spinon to propagate freely. The right plot depicts the scenario where the vison is one plaquette away, causing the spinon to oscillate between the first two stars only.

The lower panels in Fig. 2 show the simulation results from the IonQ Aria quantum device. As time evolves, the spinon propagates to the rest of the ladder in the absence of visons (bottom left panel). The leading quantum coherent oscillations<sup>6</sup> across the entire ladder (standing

<sup>3</sup> As mentioned earlier, the quantum numbers of  $B_{1,4}$  and of the string operator are inconsequential and shall not be discussed here.

<sup>4</sup> The layout of IonQ Aria quantum device is shown in Supplementary Material.

<sup>5</sup> The detail of the IonQ Aria quantum device is shown in Supplementary material

<sup>6</sup> Weaker, faster oscillations are visible in the IonQ data, as well as

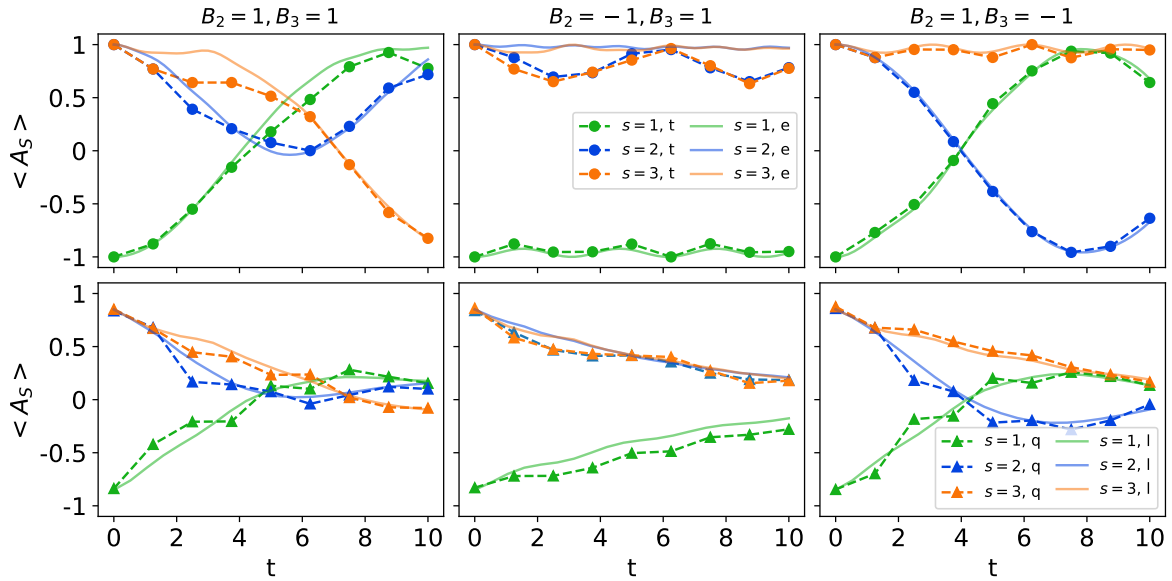


FIG. 2. A spinon propagating in the background of three vison configurations: (i) no vison,  $B_{2,3} = +1$  (left column); (ii) a single vison on the center-left plaquette,  $B_2 = -1, B_3 = +1$  (middle column); (iii) a single vison on the center-right plaquette,  $B_2 = +1, B_3 = -1$  (right column). The expectation values of star operators  $\langle A_s \rangle$  at all sites  $s = 1, 2, 3$  are calculated to track the location of the spinon. The upper panel shows the results obtained from exact diagonalization ‘e’ (solid lines) contrasted with Trotterization ‘t’ (solid circles and dashed lines). The lower panel shows the IonQ Aria simulation results ‘q’ (solid triangles and dashed lines) compared with Lindbladian dynamics ‘l’ (solid lines) with noise strength  $\gamma = 0.008$ . The IonQ results are obtained by measuring each qubit in the Pauli Z-basis. For a Toric ladder of size  $N = 8$ , we take 1000 measurement samples at each time step to calculate the expectation value  $\langle A_s \rangle$ .

wave) that are notably visible in the absence of noise (top left panel) are suppressed in the quantum device by an overall decay envelope toward a thermalized state.

Notwithstanding this, we observe clear signatures of the spinon blocking effects expected in presence of a vison in one of the central plaquettes in Fig. 2 (lower panel middle and right plots), suggesting that there is indeed enough coherence for the mutual semionic statistics to qualitatively affect spinon propagation, before the system eventually relaxes towards a maximally mixed state.

In order to understand more closely the behaviour observed in the noisy quantum environment provided by IonQ, we couple our model in Eq. (1) to a generic isotropic single-spin bath *a la* Lindblad:

$$\dot{\rho} = -i[H, \rho] + \gamma \sum_i (\sigma_i^x \rho \sigma_i^x + \sigma_i^y \rho \sigma_i^y + \sigma_i^z \rho \sigma_i^z - 3\rho) \quad (2)$$

where the sum is over all the spins, and  $\gamma$  is the bath coupling strength, whose value is chosen by visually optimising the agreement with IonQ results (see also Supplementary Material for an estimate of our confidence interval for the optimal value of  $\gamma$ ).

Note that in the IonQ simulations we are unable to attain fully coherent values  $\langle A_1 \rangle = -1$  and  $\langle A_2 \rangle = \langle A_3 \rangle = 1$ , corresponding to a spinon initialized at site  $s = 1$  at  $t = 0$ . We therefore assume that the initial states prepared in the quantum devices can only achieve a fidelity of approximately 85%, due to noise. To account for this imperfect initial state, in the Lindbladian simulations we use the working assumption that the initial density matrix of the system is a mixture:  $p\rho_0 + (1-p)\mathbb{I}/N$ , with  $p \approx 0.85$ ; here  $\rho_0$  is the pure density matrix of the desired initial state, and  $\mathbb{I}/N$  is the density matrix of a totally mixed state.

Note that an isotropic bath introduces dephasing of the spinon hopping amplitudes as well as decay in both the spinon and vison number. All processes are needed for the simulations to agree with the IonQ results. This is to be contrasted for example with the case of an anisotropic bath coupled only to the  $\sigma^z$  component of the spins (discussed for completeness in the Supplementary Material), which is only able to capture the IonQ behaviour at a qualitative level.

While our choice of bath is not drawn from any realistic attempt to describe accurately the source of noise in IonQ quantum devices, the agreement that we observe throughout the range of initial conditions and time scales probed in our work is remarkable, as shown in Fig. 2 (lower panel).

in the Trotterized solution without noise, shown in the top panels of Fig. 2. These are due to our choice of boundary conditions, which do not strictly conserve spinon number.

*Conclusion* - We devised a synthetic Mach-Zehnder interferometer, realizable in current noisy quantum devices, to probe the fractional exchange statistics of excitations in topological states of matter. Specifically, we implemented the toric ladder, a one-dimensional version of the toric code, which exhibits striking interference effects originating from mutual semionic statistics when spinons traverse different paths in the presence of visons.

Despite the device noise, we observed the interferometric signatures of the semionic statistics in the IonQ Aria quantum device. Using the Mach-Zehnder interferometer to detect fractional statistics has several advantages. Foremost, the statistical signatures emerge naturally in the nonadiabatic quantum evolution of the system generated by a time-independent Hamiltonian that supports the topological state, obviating the need for intricate control to mimic adiabatic braiding dynamics. Furthermore, extracting the signatures of the exchange statistics requires no auxiliary qubits coupled to the systems, unlike the approach adopted by the Google group [19].

Beyond serving as an alternative synthetic platform for investigating anyonic statistics relevant to spin liquids, our findings offer insight into quantum computing devices' coherence length and timescales. This goal is achieved by directly examining the decay rate of spinon blockage, a phenomenon that would persist indefinitely in a noise-free system. Comparing our quantum hardware results with numerical calculations, we have validated the accuracy of a Lindbladian noise model in capturing the noise characteristics of the IonQ device.

*Acknowledgement* - We are grateful to Orazio Scarlatella for many useful discussions and for generously sharing with us his expertise on open quantum systems and Lindblad evolution. A.R. thanks Boston University's Physics Department for hospitality. This work was funded in part by the Engineering and Physical Sciences Research Council (EPSRC) grants No. EP/T028580/1 and No. EP/V062654/1 (C.C.), by DOE Grant No. DE-FG02-06ER46316 (C.Ch.), and by NSF Grant No. DMR-1945395 (A.R.). Research at Perimeter Institute is supported in part by the Government of Canada through the Department of Innovation, Science and Industry Canada and by the Province of Ontario through the Ministry of Colleges and Universities.

- 
- [1] A. A. Michelson and E. W. Morley, *American Journal of Science* **s3-34**, 333 (1887).
- [2] A. Perot and C. Fabry, *The Astrophysical Journal* **9**, 87 (1899).
- [3] C. Fabry and A. Perot, *The Astrophysical Journal* **13**, 265 (1901).
- [4] B. P. Abbott and et al. (LIGO Scientific Collaboration and Virgo Collaboration), *Phys. Rev. Lett.* **116**, 061102 (2016).
- [5] J. Nakamura, S. Liang, G. C. Gardner, and M. J. Manfra, *Nature Physics* **16**, 931 (2020).
- [6] J. Nakamura, S. Liang, G. C. Gardner, and M. J. Manfra, *Nature Communications* **13**, 10.1038/s41467-022-27958-w (2022).
- [7] J. Nakamura, S. Liang, G. C. Gardner, and M. J. Manfra, *Phys. Rev. X* **13**, 041012 (2023).
- [8] K. T. Law, D. E. Feldman, and Y. Gefen, *Phys. Rev. B* **74**, 045319 (2006).
- [9] N. Batra, Z. Wei, S. Vishveshwara, and D. E. Feldman, *Physical Review B* **108**, 10.1103/physrevb.108.1241302 (2023).
- [10] H. K. Kundu, S. Biswas, N. Ofek, V. Umansky, and M. Heiblum, *Nature Physics* **19**, 515 (2023).
- [11] R. Moessner and E. J. Moore, *Topological Phases of Matter* (Cambridge University Press, 2021).
- [12] A. Kirmani, K. Bull, C.-Y. Hou, V. Saravanan, S. M. Saeed, Z. Papić, A. Rahmani, and P. Ghaemi, *Phys. Rev. Lett.* **129**, 056801 (2022).
- [13] A. Kirmani, D. S. Wang, P. Ghaemi, and A. Rahmani, *Phys. Rev. B* **108**, 064303 (2023).
- [14] A. Lopez-Bezanilla, J. Raymond, K. Boothby, J. Carrasquilla, C. Nisoli, and A. D. King, *Nature Communications* **14**, 10.1038/s41467-023-36760-1 (2023).
- [15] Z. Wei, V. F. Mitrović, and D. E. Feldman, *Phys. Rev. Lett.* **127**, 167204 (2021).
- [16] Z. Wei, N. Batra, V. F. Mitrović, and D. E. Feldman, *Phys. Rev. B* **107**, 104406 (2023).
- [17] J. Knolle and R. Moessner, *Annual Review of Condensed Matter Physics* **10**, 451–472 (2019).
- [18] C. Broholm, R. J. Cava, S. A. Kivelson, D. G. Nocera, M. R. Norman, and T. Senthil, *Science* **367**, 10.1126/science.aay0668 (2020).
- [19] K. J. Satzinger, Y.-J. Liu, A. Smith, C. Knapp, M. Newman, C. Jones, Z. Chen, C. Quintana, X. Mi, A. Dunsworth, C. Gidney, I. Aleiner, F. Arute, K. Arya, J. Atalaya, R. Babbush, J. C. Bardin, R. Barends, J. Basso, A. Bengtsson, A. Bilmes, M. Broughton, B. B. Buckley, D. A. Buell, B. Burkett, N. Bushnell, B. Chiaro, R. Collins, W. Courtney, S. Demura, A. R. Derk, D. Epens, C. Erickson, L. Faoro, E. Farhi, A. G. Fowler, B. Foxen, M. Giustina, A. Greene, J. A. Gross, M. P. Harrigan, S. D. Harrington, J. Hilton, S. Hong, T. Huang, W. J. Huggins, L. B. Ioffe, S. V. Isakov, E. Jeffrey, Z. Jiang, D. Kafri, K. Kechedzhi, T. Khattar, S. Kim, P. V. Klimov, A. N. Korotkov, F. Kostritsa, D. Landhuis, P. Laptev, A. Locharla, E. Lucero, O. Martin, J. R. McClean, M. McEwen, K. C. Miao, M. Mohseni, S. Montazeri, W. Mruczkiewicz, J. Mutus, O. Naaman, M. Neeley, C. Neill, M. Y. Niu, T. E. O'Brien, A. Opremcak, B. Pató, A. Petukhov, N. C. Rubin, D. Sank, V. Shvarts, D. Strain, M. Szalay, B. Villalonga, T. C. White, Z. Yao, P. Yeh, J. Yoo, A. Zalcman, H. Neven, S. Boixo, A. Megrant, Y. Chen, J. Kelly, V. Smelyanskiy, A. Kitaev, M. Knap, F. Pollmann, and P. Roushan, *Science* **374**, 1237–1241 (2021).
- [20] G. Semeghini, H. Levine, A. Keesling, S. Ebadi, T. T. Wang, D. Bluvstein, R. Verresen, H. Pichler, M. Kalinowski, R. Samajdar, A. Omran, S. Sachdev, A. Vishwanath, M. Greiner, V. Vuletić, and M. D. Lukin, *Science* **374**, 1242–1247 (2021).
- [21] A. Kitaev, *Annals of Physics* **303**, 2 (2003).
- [22] O. Hart, Y. Wan, and C. Castelnovo, *Phys. Rev. B* **101**, 064428 (2020).

- [23] O. Hart, Y. Wan, and C. Castelnovo, [Nature Communications](#) **12**, 1459 (2021).
- [24] S. Zhou, M. Zelenayova, O. Hart, C. Chamon, and C. Castelnovo, [SciPost Physics](#) **15**, 194 (2023).

## Supplementary Material

### IONQ QUANTUM DEVICE LAYOUT

The IonQ quantum devices are ion-based digital quantum machines where qubits are made of ionized ytterbium atoms and have all-to-all connectivity [1]. Our demonstration is implemented using the IonQ Aria device, accessible through the AWS Braket (specifically Aria 1). With a total of 25 qubits, the Aria quantum device supports the majority of common quantum gates which can be translated into their native gates. Its average 1-qubit and 2-qubit gate fidelities are about 99.04% and 99.40%, and the average durations for 1-qubit and 2-qubit gate are roughly  $135 \mu\text{s}$  and  $600 \mu\text{s}$ , respectively. The T1 time is reported to range from 10 s to 100 s, and the T2 time is approximately 1 s [2].

### OPTIMAL TROTTERISATION

Here we elaborate on the derivation of the optimal number of Trotter steps,  $n_{\text{opt}}$ , used in the quantum device implementation. The selection of this optimal number takes into account two considerations: 1) the Trotter approximation error tends to 0 in the limit of large number of Trotter steps; 2) the noisy nature of quantum devices gives a preference for shallow circuits, and therefore small number of Trotter steps, to reduce loss of coherence / thermalisation. In an attempt to balance these two conflicting trends, we look for an optimal number of Trotter steps,  $n_{\text{opt}} = 8$  for a time evolution up to  $T = 10$ , in order to achieve sufficient accuracy ( $\lesssim 15\%$ ) with contained accumulated noise.

In Fig. 1, we show the Trotter approximation error as a function of the number of Trotter steps  $n$ . The error is calculated by taking the absolute value of the difference between  $A_s^{(e)}(t)$  evaluated from the exact diagonalization and  $A_s^{(t)}(t)$  from the Trotterization, averaged over all three sites  $s = 1, 2, 3$  and three visons configurations: (1)  $B_2 = B_3 = 1$ ; (2)  $B_2 = -1, B_3 = 1$ ; (3)  $B_2 = 1, B_3 = -1$ , with the spinon initialized at  $s = 1$ . As expected, the Trotter error gradually decays to 0 as  $n$  increases. We choose 15% as a working error threshold and we see that this is achieved for  $n \geq 8$ , which we then use as our optimal number of Trotterisation steps.

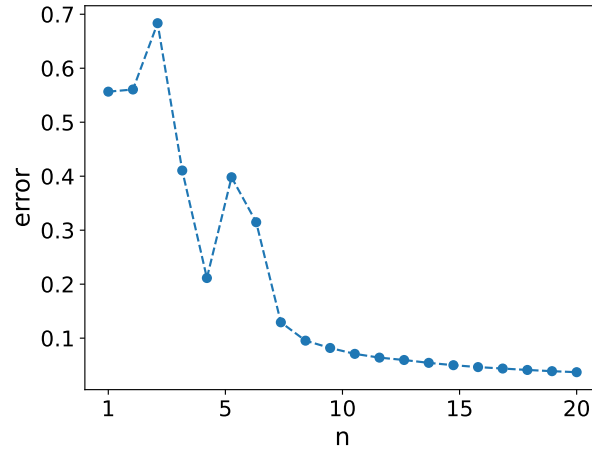


FIG. 1. The Trotter approximation error versus the number of Trotter steps  $n$ . The error decrease with significant fluctuations down to about 0.129 at  $n = 8$ , and smoothly decays toward 0 as  $n$  keeps increasing.

### LINDBLAD EVOLUTION

We effectively model the noise in the quantum device IonQ by introducing independent Markovian heat baths to each spin, described by the Lindblad Master equation. Under the assumption of isotropic noise in spin space, the

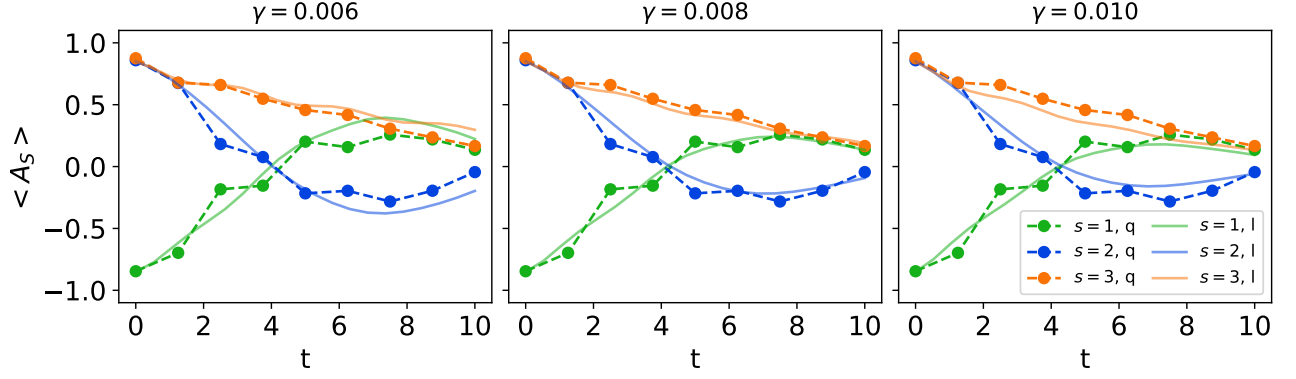


FIG. 2. Comparison of the IonQ simulations against the Lindblad results for the time evolution of the expectation value of the star operators at  $s = 1, 2, 3$ , effectively tracking the position of the spinon initially prepared at  $s = 1$ , as a function of time. We show the comparison for three values of the Lindblad coupling to the bath,  $\gamma = 0.006$  (left panel),  $\gamma = 0.008$  (central panel), and  $\gamma = 0.010$  (right panel), for the case where a vison is initially placed on the centre-right plaquette. The same initial conditions as in the main text were used here.

corresponding Lindblad equation, Eq. 2 in the main text, is given by

$$\dot{\rho} = -i[H, \rho] + \gamma \sum_i (\sigma_i^x \rho \sigma_i^x + \sigma_i^y \rho \sigma_i^y + \sigma_i^z \rho \sigma_i^z - 3\rho)$$

where the sum is over all the spins, and  $\gamma$  is the coupling strength to the bath.

The main difficulty in simulating this equation lies in the presence of both operators acting to the left and to the right of  $\rho$ , preventing any factorisation of the right hand side that could transform it into a matrix eigenvalue problem. To overcome this, we introduce the vectorised form of the density matrix  $\vec{\rho}$  by stacking the rows of its matrix representation. The Lindblad equation is then recast as:

$$\dot{\vec{\rho}} = \left\{ -i(H \otimes I - I \otimes H^T) + \gamma \sum_i [\sigma_i^x \otimes (\sigma_i^x)^T + \sigma_i^y \otimes (\sigma_i^y)^T + \sigma_i^z \otimes (\sigma_i^z)^T - 3I \otimes I] \right\} \vec{\rho} = \mathcal{L} \vec{\rho}, \quad (1)$$

where  $\otimes$  denotes the standard matrix tensor product, and  $\mathcal{L}$  is sometimes referred to as the Lindbladian superoperator. Now that the Master equation is put into this new form, the vectorised density matrix  $\vec{\rho}$  can be trivially evolved in the eigenbasis of  $\mathcal{L}$  and can then be reshaped into the conventional matrix form  $\rho$ .

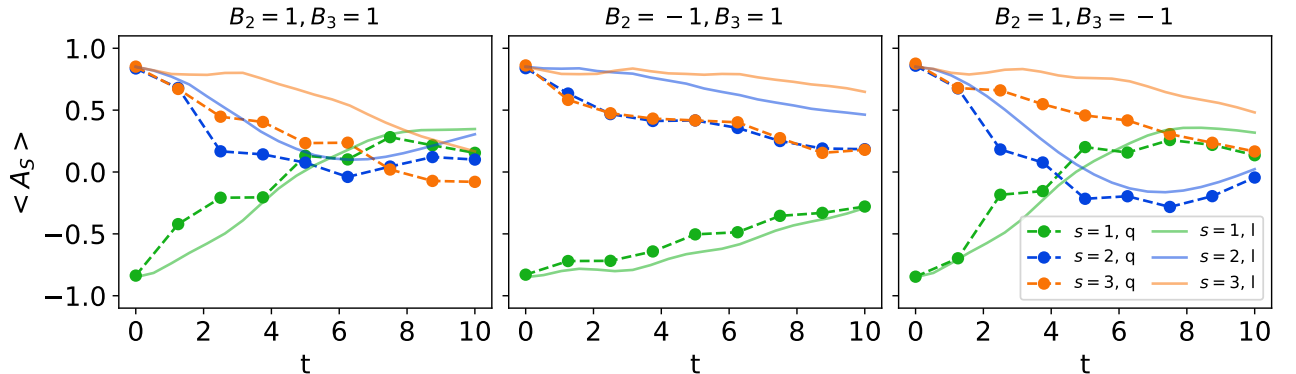


FIG. 3. Comparison of the IonQ simulations against the Lindblad evolution with the bath coupled only to the  $\sigma_z$  component of the spins. The best agreement occurs visually for  $\gamma = 0.05$ , which is used in these plots. The absence of  $\sigma_x$  and  $\sigma_y$  dephasing gives rise to a more prominent spinon confinement in presence of a vison, resulting in a worse fit compared to the isotropic case. The initial conditions used here are the same as the three isotropic cases.

## LINDBLAD PARAMETERS

In the main text, we showed a comparison between our Lindblad results for bath coupling strength  $\gamma = 0.008$  and IonQ simulations in main text Fig. 3. For the purpose of this work, we did not attempt to systematically obtain the best fit value for  $\gamma$  but we rather used a visual estimate. A sense of the accuracy of our comparison can be derived from Fig. 2, where we show how the agreement worsens if we either decrease or increase the value of  $\gamma$  (for simplicity, we show here only one choice of initial conditions, namely the case of a vison on the centre-right plaquette). It is therefore sensible to assume  $\gamma = 0.008 \pm 0.001$ .

For completeness, we show in Fig. 3 also the case of an anisotropic bath that couples only to the  $\sigma^z$  component of the spins (with coupling strength  $\gamma = 0.05$ , visually estimated to give the best agreement with the IonQ results).

Such bath acts as dephasing to the spinon motion; around the plaquette this effect can be equivalently described and understood as vison number decay. Spinon number decay only occurs in this case at the ladder boundaries (in the absence of other spinon number non-conserving channels provided by bath coupling to  $\sigma_x$  and  $\sigma_y$ ). We see a qualitatively similar behaviour, although the isotropic bath case captures the IonQ behaviour noticeably better (see main text Fig. 3).

---

[1] Ionq, <https://ionq.com/technology> (), copyright © 2017-2024 IonQ, Inc.

[2] Ionq aria, <https://ionq.com/quantum-systems/aria> (), copyright © 2017-2024 IonQ, Inc.